Proceedings of the 7th International Conference on HydroScience and Engineering

Philadelphia, USA September 10-13, 2006 (ICHE 2006)

ISBN: 0977447405

Drexel University

College of Engineering

3D LES COMPUTATIONS OF A SHALLOW LATERAL EXPANSION USING AN IMMERSED BOUNDARY METHOD

Harmen Talstra[1], Wim S.J. Uijttewaal[2] and Guus S. Stelling[3]

ABSTRACT

In environmental shallow flows, the phenomenon of flow separation often gives rise to large-scale turbulent structures (vortex shedding). In this study, 3D LES computations of three Shallow Lateral Expansion geometries are performed. The resolved large-scale turbulent structures are studied in detail in order to allow a comparison with laboratory experiments, carried out using the Particle Image Velocimetry (PIV) technique. When LES is applied for practical cases involving flow separation, immersed boundaries are often an essential part of the geometry. These boundaries can cause problems with respect to the Navier Stokes solver used, especially regarding the pressure correction module. A solution to this problem, known as Immersed Boundary Method (IBM), is found by using body forces to ensure the impermeability of internal boundaries. In this study an alternative implementation of a Direct Forcing IBM is proposed, based on momentum fluxes instead of body forces. This model is applied to Shallow Lateral Expansion geometries of various aspect ratios. In order to analyze the real-time large-scale turbulent structures, the vector potential function of the velocity field is computed. This is a very suitable tool to detect large-scale flow structures. The turbulence features observed in the 3D LES computation are compared with the PIV data, especially regarding the vortex shedding behaviour. An analysis of Reynolds stresses and the downstream development of eddy length scales reveals the existence of two different regimes in the vortex shedding behaviour. The difference can be explained by the interaction of shed vortices with the primary and secondary recirculation cells that are present.

1. INTRODUCTION

1.1 Background and objective

Shallow flows in which flow separation plays a role are abundant in the natural environment. In rivers, for example, flow separation past obstacles or expansions often gives rise to large-scale coherent structures that bear typical characteristics of quasi two-dimensional turbulence. In practice, these coherent structures may cause problems regarding e.g. navigation and bed erosion. Environmental shallow flows, like rivers, are being utilized for lots of purposes: e.g. water

[1] PhD student, Faculty of Civil Engineering and Geosciences, Delft University of Technology, The Netherlands
[2] Associate Professor, Faculty of Civil Engineering and Geosciences, Delft University of Technology, The Netherlands
[3] Professor, Faculty of Civil Engineering and Geosciences, Delft University of Technology, The Netherlands

discharge, navigation, transport, ecological values. These purposes may often conflict. For an optimal river management, it is necessary to know with some accuracy what effects will occur if the flow system is changed by human intervention. Because shallow flow turbulence can affect navigation as well as sediment transport and mixing of conveyed material, improving the understanding and modelling of large-scale turbulence in shallow flows is of practical relevance.

The turbulent flow studied here has two key characteristics. First, the flow is shallow, i.e. the water depth is much smaller than the dominant horizontal flow length scales (typical aspect ratio 5% or less). Therefore, most of the large-scale turbulence may be considered as quasi two-dimensional. Second, the flow is separating: due to an adverse pressure gradient the main flow separates from a wall, inducing a zone of flow recirculation and often a street of coherent structures emerging from the separation point (vortex shedding). Both key characteristics come together in many rivers and coastal flow geometries.

In this study, three-dimensional Large Eddy Simulations (LES) are performed in order to study the behaviour of large-scale shed vortices in a simple shallow separation flow geometry, the Shallow Lateral Expansion (SLE). Obviously, a 3D LES computation is a useful tool for a real-time study of the dynamics of individual large eddies. In this way, a good comparison can be made with existing laboratory data. These data have been acquired from shallow flow experiments carried out using the measurement technique of Particle Image Velocimetry (PIV). These experiments are described in Talstra, Uijttewaal & Stelling (2006). The vortex shedding phenomenon, as indicated by the experimental data, is expected to be found back within the LES data. The acquired experimental and numerical information is being used to inspire further development of simpler numerical models useful for shallow flow geometries in which separation plays a role.

1.2 Previous experimental results

Figure 1 shows a perspective view of a shallow separating flow past an expansion, visualised by the injection of dye (located at the shallow flow facility of the Environmental Fluid Mechanics Laboratory, Delft University of Technology). Behind the lateral expansion, the separation gives rise to a primary and secondary recirculation cell. This is a well-known flow pattern, reported many times in literature; see e.g. Babarutsi, Nassiri & Chu (1996). At the interface between main flow and recirculation zone, lateral exchange of momentum and dissolved matter takes place due to the presence of large-scale coherent structures. The presence of steady recirculation zones makes the flow behaviour different from that of a plane horizontal mixing layer with only a lateral velocity difference.

In their experimental study on shallow groyne fields, Uijttewaal, Lehman & Van Mazijk (2001) observed a qualitative difference between two types of large-scale structures: firstly mixing layer vortices, and secondly coherent structures that are larger in scale. The latter type of structures is associated with the interaction with the secondary recirculation cell, while the first type is associated with lateral shear instabilities.

From the experimental PIV study of Talstra, Uijttewaal & Stelling (2006), the difference between these two large eddy types can be clarified. The experimental setup (which is identical to the geometry of the 3D LES computations) will be described in Section 2.1.

In the initial stage of a developing shallow separating flow, no secondary gyre does exist; the primary gyre fills the entire expansion area. The lateral velocity difference between mean flow and recirculation zone is small and gradually changing, so that relatively weak and gentle mixing layer eddies are present. As soon as the secondary recirculation has sufficiently developed, the initial mixing layer changes character and much larger vortices are shed than before. It is observed that the largest eddy scales are emerging not from the separation point, but from a point some distance downstream – approximately at the point where the mixing layer starts to be influenced by the primary recirculation. In this area a sudden increase in vortex sizes is visible, which is labeled here

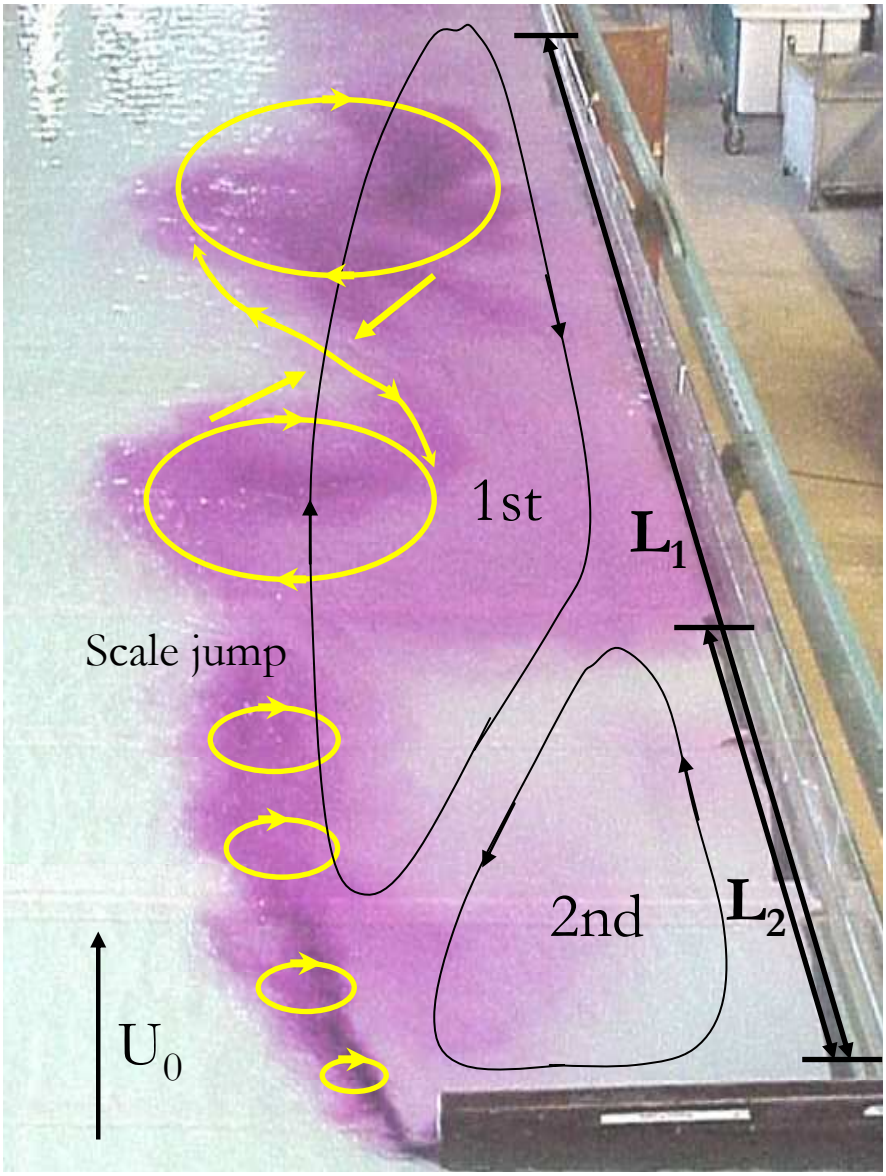

Figure 1 Large-scale structures in a shallow separating flow, visualised by dye. Shown are: main flow direction (U), steady primary recirculation (1st), steady secondary recirculation (2nd), and the approximate "scale jump" location. In yellow: spatial structure of the mixing layer eddies

as "scale jump". Between the far-field coherent structures downstream from the scale jump location, the velocity field is stretched in diagonal streamwise direction and compressed in the direction perpendicular to it (saddle points). At these spots strong vortex stretching takes place due to the velocity field deformation, resulting in long streaks of strong upwelling and downwelling of fluid.

The scale jump phenomenon can be explained by the way the shallow mixing layer interacts with both steady recirculations. If the flow geometry is such that a large and well-developed secondary recirculation exists, the secondary return flow comes very close to the streamwise main flow immediately downstream of the separation point. At this location a considerable lateral shear is present. From this point on, a mixing layer starts to grow. The size of mixing layer eddies, however, remains small because the mixing layer is confined between main flow and the secondary recirculation. At the point downstream where the mixing layer starts to be influenced by the primary recirculation, the lateral shear is much lower. From that point on, there is a positive interaction between mixing layer eddies and the primary recirculation. It appears that much larger eddies are

being formed. This can be explained from the concept of “vortex merging”: quasi two-dimensional vortices with the same vorticity sign are known to merge, while vortices of opposite vorticity sign tend to coexist without much interaction. Indeed, instantaneous velocity fields from the PIV experiments show merging of mixing layer structures with the primary recirculation.

As (in a shallow separating flow) the primary recirculation has the same vorticity sign as mixing layer eddies, while the secondary recirculation has the opposite sign, two different spatial regimes can be distinguished. Consequently, the two distinct large eddy types as observed by Uijttewaal, Lehman & Van Mazijk (2001) represent an internal flow phenomenon: the different interaction of shed vortices with two steady recirculations.

The scale jump phenomenon can be ascribed to the quasi two-dimensional character of the considered flow geometry. Although vortex shedding also occurs within the context of Backward Facing Step flow with infinite spanwise extent (a geometry which has been extensively studied in literature, see e.g. Neto *et al*, 1993), the behaviour of shed vortices there is quite different from a shallow expansion. Due to three-dimensionality the shed vortices are breaking up rapidly and their turbulent kinetic energy does not shift to larger scales, this in contrast with a shallow separating flow.

2. DESCRIPTION OF 3D-LES EXPERIMENTS

2.1 Geometry and numerical setup

Figure 2 and 3 show the three flow geometries, which are almost identical for LES computations and PIV experiments, both in shape and scale. The laboratory setup has a length of 20.00m, a width of 2.00 m and a water depth of 92 mm. The outflow width b_2 is 2.00m in all three cases; the inflow width b_1 is 0.50, 1.00 or 1.50 m. The inflow/outflow width ratio b_1/b_2 is respectively 1:4, 2:4 and 3:4. The lateral expansion width d_1 is defined as: $d_1 = b_2 - b_1$. The length of the inflow section is 5.00 m in order to ensure a sufficiently developed turbulent flow. The dimensions of the numerical LES setup resemble those of the PIV experiments; the three cases are referred to as the *1:4*, *2:4* and *3:4* geometry. The LES setup length, however, is made 30.00 m. By doing this, it can be assumed that the numerical outflow boundary condition has hardly any effect on the turbulent flow.

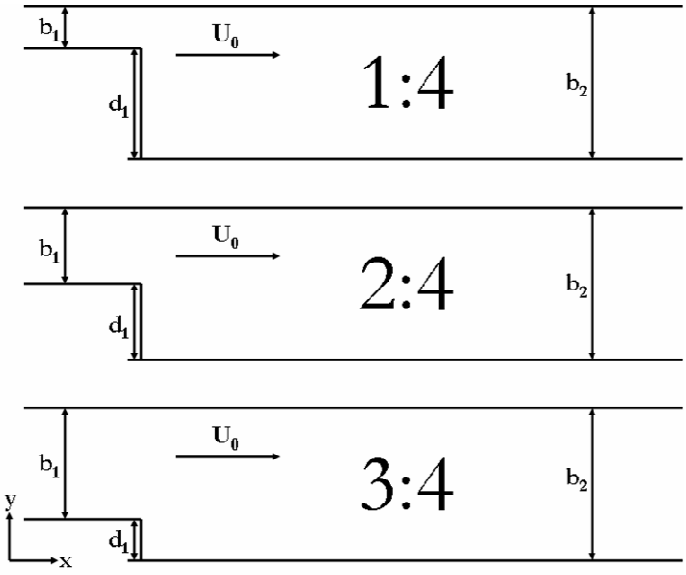

Figure 2 Overview of the three PIV and LES geometries (1:4, 2:4 and 3:4 case)

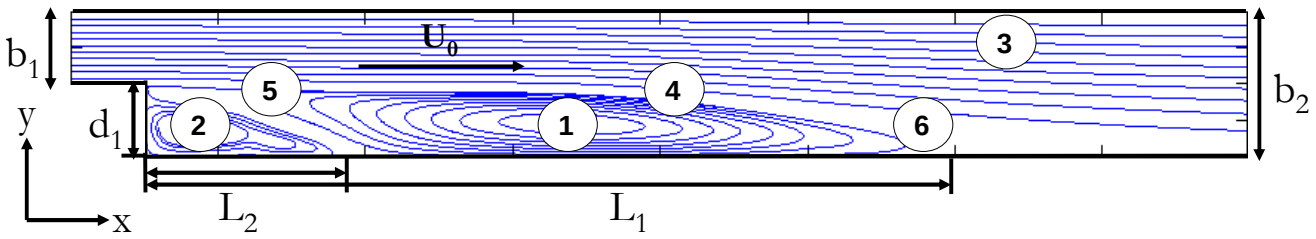

Figure 3 Sketch of the 2:4 geometry with time-averaged streamlines. Location of expected flow features: 1) primary recirculation, 2) secondary recirculation and secondary separation point, 3) intermittent opposite recirculation, 4) far-field mixing layer, 5) near-field mixing layer, 6) primary reattachment point

The LES solver being used is a finite volume formulation with a predictor-corrector algorithm (pressure correction). The computational mesh is a uniform Cartesian grid consisting of 1200 x 80 x 16 cells. The 1:4 and 2:4 cases have horizontal mesh size of 0.025 m and a computational time step of 0.01 s, ensuring a maximum Courant number of about 0.40. In the 3:4 case, both the horizontal spatial and the temporal resolution are doubled in order to maintain a sufficiently high resolution to resolve the secondary recirculation cell. In the main flow, the dimensionless wall-normal distance y^+ has a typical value between 30 and 45; within the recirculation areas, it is usually lower. Output data of the turbulent velocity field are stored with a sampling frequency of 10 Hz (the PIV sampling frequency is 9.67 Hz). The sampling duration is 10000 frames (1000 s). The set of equations solved are the 3D incompressible Navier-Stokes equations and a straightforward Smagorinsky formulation (without Van Driest damping) to account for the subgrid-scale stresses. The used Smagorinsky constant has a value of 0.10. Instead of a free surface, a free-slip rigid lid boundary condition has been used.

The uniform inflow velocity U_0 is 0.30 m/s; the far-field Reynolds number (based on the water depth and the average main flow velocity) varies between 7500 and 22500. Like in the experiments, the computational inflow boundary lies at 5.00 m upstream of the separation point. At this inflow plane, random velocity disturbances are imposed, having a maximum of 5% of the (uniform) inflow velocity U_0. This is done in order to trigger 3D bottom turbulence conditions similar to the experimental situation.

The open inflow boundary condition is of the Dirichlet type; a Neumann-type outflow boundary condition (with respect to the predicted velocity field) has been used. Wall shear stresses at bottom and sidewalls are imposed by means of surface forces, acting on those grid cell boundaries where impermeable walls are present. Any arbitrary labyrinth of dry grid cells and thin dams can be handled in this way without any need for “mirror velocity points” at boundaries (which are sometimes used in order to impose velocity gradients on solid walls). Of course, the use of wall functions for LES computations is quite common; however, it is emphasized here that the use of surface forces is to be preferred above the use of mirror points, because it is more generic. The wall function includes no-slip region, buffer layer and logarithmic layer (partial slip) and reads:

$$\begin{aligned} u^+ &= y^+, && 0 \le y^+ < 5 && \text{(viscous sublayer)} \\ u^+ &= -2.90 + 4.91 \cdot \log(y^+), && 5 \le y^+ < 27.5 && \text{(buffer layer)} \\ u^+ &= 5.29 + 2.44 \cdot \log(y^+), && y^+ \ge 27.5 && \text{(logarithmic layer)} \end{aligned} \qquad (1)$$

with

$$u^+ = u_1 / u_* \quad \text{and} \quad y^+ = u_* y_1 / \nu \qquad (2)$$

where y_1 is the distance of the first velocity point from the wall, u_1 is the near-wall flow velocity, u_* is the friction velocity, ν is the kinematic viscosity, y^+ is the dimensionless wall-normal distance and u^+ is the number of velocity units (in the formulation above, "y" can stand for x or y in case of the horizontal distance from a sidewall, or z in case of a vertical distance from the bottom). Actually, the formulations above assume a fully developed turbulent boundary layer along solid walls. This is obviously not correct for separation regions. However, in the neighbourhood of secondary separation points (the most critical zones in this study) the near-wall velocities are very small; hence the first grid point is close enough to the wall to allow for the application of a no-slip boundary condition, which is correct regardless how well the boundary layer has been developed.

The predictor module of the applied Navier-Stokes solver uses a second-order Adams-Bashfort discretisation in time and a central differencing scheme in space to account for the momentum advection. Within the pressure correction module, the 3D Poisson equation system is solved by cosine transformations in the horizontal plane (or Fast Fourier Transformations in periodical cases) and Gaussian elimination in the vertical direction.

2.2 On immersed boundaries; an alternative IBM formulation

Internal (immersed) boundaries are often an essential part of flow geometries, especially for cases involving flow separation. Therefore it is required that a LES formulation must be able to satisfy boundary conditions at any location within the interior of the model. The latter, however, is not straightforward for the efficient kind of LES solver that is described above, i.e. a solver using FFT or cosine transformations. Internal impermeable walls directly influence the way in which the 3D Poisson matrix system of the pressure correction module can be solved. Internal boundaries cause this matrix to have a non-standard form and hence introduce non-standard eigenvalues. An FFT-type solving procedure for the Poisson matrix becomes impossible, which implies that other and less efficient solution methods are required, considerably increasing the computational effort.

A common and effective solution to this problem, known as the Immersed Boundary Method (IBM), is to maintain the standard 3D Poisson matrix structure, and applying the internal boundary conditions to the predictor module only; see e.g. Fadlun et al. (2000) or Breugem (2004) for a general description. To this end, body forces are imposed on immersed boundaries in order to ensure wall impermeability. This can be done iteratively (Feedback Forcing) or immediately (Direct Forcing). Due to the application of the standard Poisson matrix structure, small residual normal-wall velocities will remain. These errors can be minimized by updating the pressure every time step: $p^{n+1} = p^n + \hat{p}$ (see Breugem, 2004). After some simulation time, as soon as the influence of initial conditions has disappeared, the residual velocities are often much smaller than the mean flow velocity (a difference of many orders of magnitude) and can therefore be neglected. The general Direct Forcing numerical scheme reads:

$$\hat{u}_i = u_i^n + \Delta t\left(-RHS_i^n + f_i^n\right), \tag{3a}$$

$$\text{where: } RHS_i = \frac{\partial u_i u_j}{\partial x_j} + \frac{1}{\rho}\frac{\partial p}{\partial x_i} - \frac{\partial}{\partial x_j}\nu\left(\frac{\partial u_i}{\partial x_j} + \frac{\partial u_j}{\partial x_i}\right), \tag{3b}$$

$$\frac{\Delta t}{\rho}\frac{\partial^2 \hat{p}}{\partial x_i^{\,2}} = \frac{\partial \hat{u}_i}{\partial x_i}, \tag{3c}$$

$$u_i^{n+1} = \hat{u}_i - \frac{\Delta t}{\rho}\frac{\partial \hat{p}}{\partial x_i}, \text{ and} \tag{3d}$$

$$p^{n+1} = p^n + \hat{p} \tag{3e}$$

where $\hat{u}$ is the predictor velocity, $\hat{p}$ is the pressure update, f is the body force at solid wall boundaries, Δt is the time step, i is the dimensional direction and n is the time level. The RHS accounts for the explicit terms in the equation system: the convective and diffusive terms as well as a predictor pressure gradient. These can be computed according to either an Euler-Explicit of Adams-Bashfort numerical scheme. Figure 4 illustrates the action of body forces at some arbitrary boundaries on a rectangular computational grid.

An extra effect of the application of an IBM, often encountered in literature, is the possibility to compute complex flow geometries on a simple rectangular grid by means of interpolation of velocities and body forces (e.g. ghost-cell IBM or cut-cell IBM). Fadlun et al. (2000) and Mittal & Iaccarino (2005) give an extensive overview of the available variety of IBM implementations. Tessicini et al. (2002) describe an application of Direct Forcing IBM to 3D LES computation in combination with an advanced boundary layer equation. Breugem (2004) applies Direct Forcing IBM to a Direct Numerical Simulation of a flow through a porous (permeable) medium.

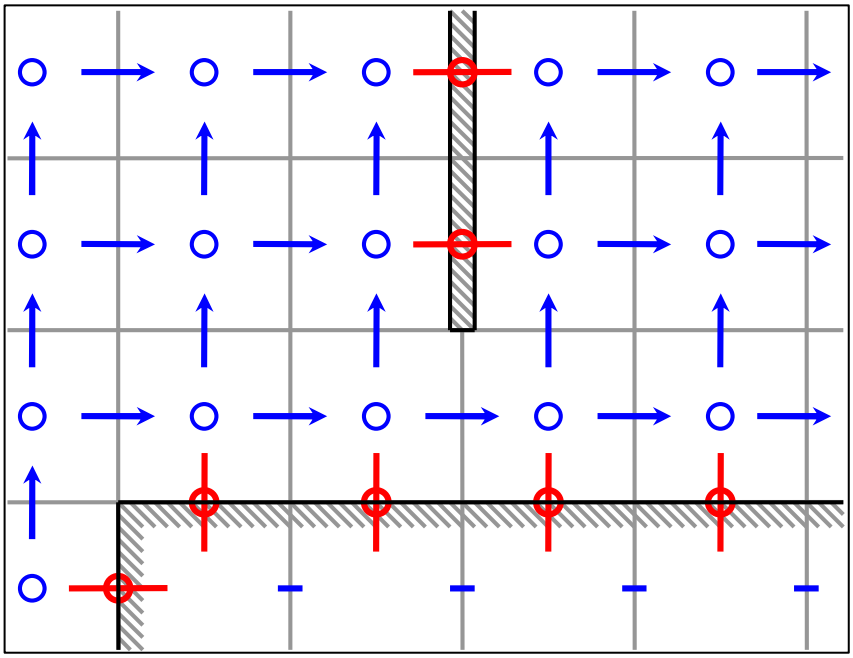

Figure 4 Action of body forces at impermeable walls in a computational grid. Blue: location of pressure points and velocity vectors. Red: location of normal-wall body forces ensuring wall impermeability

In this study, the IBM Direct Forcing formulation is implemented in an alternative way. The implementation is strongly correlated with the implementation of the wall function described in Section 2.1. No body forces are used; at solid walls, wall-normal fluxes of wall-parallel momentum are put to zero. In equation 3a, the term RHS_i^n consists of the divergence of momentum fluxes (due to convection and viscosity) in all directions; fluxes across solid walls must be cancelled. Hence, the body force f_i^n is not imposed separately on the predicted velocity field $\hat{u}_i$, but is "immersed" into RHS_i^n itself, so that the term f_i^n becomes unnecessary. In this way conservation of momentum is achieved *a priori*, instead of making a correction *a posteriori*. Also, the wall impermeability at immersed boundaries remains guaranteed.

Please note that this method is only applied to wall-normal fluxes of wall-parallel momentum. Wall-normal fluxes of wall-normal momentum, on the other hand, are being maintained. These fluxes may never be put to zero, because they represent flow forces acting on solid structures, e.g. at

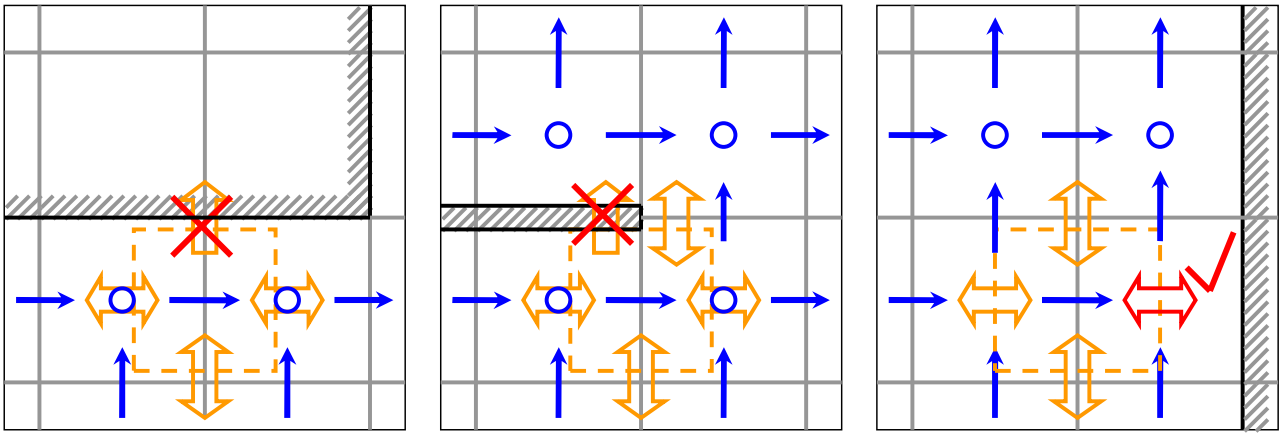

Figure 5 Illustration of alternative IBM approach. Left: normal-wall flux of wall-parallel momentum is set to zero. Middle: flux is cancelled only proportional to blocking ratio. Right: normal-wall flux of normal-wall momentum is being maintained

stagnation points. If these fluxes are set to zero nonetheless, severe numerical instabilities at stagnation points do appear. The alternative method is illustrated in Figure 5 for three different cases of grid-aligned walls: a wall parallel to the main flow, a thin dam and a wall normal to a flow (stagnation point).

2.3 Large eddy visualisation using vector potential functions

A topic requiring special attention is the way in which large-scale eddies can be detected and visualized. Although a look at the velocity field often reveals the presence of these large eddies, it is not always easy to define a straightforward detection algorithm. Bonnet et al. (1998), Scarano et al. (1999), Adrian et al. (2000) and Van Prooijen (2004) describe a variety of commonly used identification methods for coherent structures, e.g. based on vorticity, swirling strength or spatial correlations. The drawback of the latter method is the spatial inflexibility of the results; the former methods have the disadvantage that they are quite sensitive to noise, like all gradient-based methods, because they tend to enhance the importance of the smallest length scales.

In this study, the *vector potential function* of a velocity field is used to detect large eddies. The use of vector potentials is not common within the context of fluid dynamics. Yet, vector potentials are very elegant in use because they allow large vortex scales to be determined directly from instantaneous flow kinematics. They very much resemble the concept of 2D stream functions, but are computed in an alternative way in order to make a correction for the divergence of a 2D plane within a 3D velocity field. Vector potentials can be constructed by solving a Poisson equation for each separate component of the vorticity, using homogeneous Neumann boundary conditions. See the appendix for a full explanation.

Each local maximum or minimum of a vector potential field uniquely identifies a large-eddy core of positive, respectively negative vorticity. The shape of the eddy is given by the surrounding isolines, which approximately coincide with local flow velocity vectors (see Figure 6).

When vector potentials are applied to separating and recirculating flows, the permanently present primary and secondary recirculation cells are dominant; therefore, intermittent large mixing layer eddies will not be very visible. When the time-averaged flow pattern is subtracted from the instantaneous pattern, however, the residual vector potential function will show a streamwise sequence of large vortices being shed from the separation point.

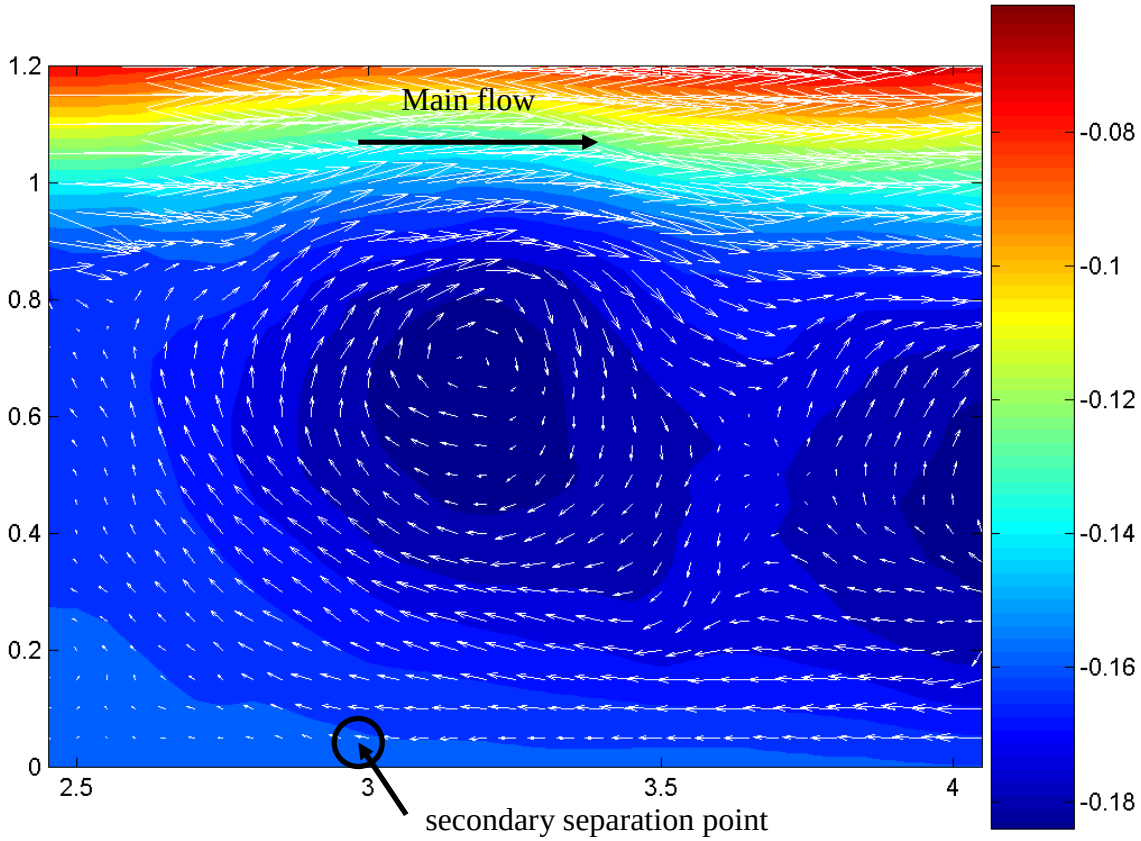

Figure 6 Detection of large-scale eddies by means of a vector potential function. White vectors visualize the instantaneous velocity field at 3 m downstream of separation point. The upper part shows the main flow (from left to right); the lower part shows the primary recirculation backflow and a secondary separation point

3. RESULTS

3.1 General flow features

A good comparison can now be made between the LES computations and PIV experiments for the 3 geometries. Within the experimental context, more data have been obtained than with the 3 PIV cases shown here: altogether 18 flow cases have been studied by visual observation. Three of these cases have been selected for comparison with computational data (see Figure 2 and Section 2.1). Some general features of both PIV data and LES data are summarized here; for a more elaborate description see Talstra, Uijttewaal & Stelling (2006).

First, a decreasing dimensionless depth h/d_1 yields a shorter primary recirculation cell: in very shallow cases the reattachment length L_1 decreases and scales with water depth, while for deeper cases the maximum reattachment length is of the order of $L_1 = 8 \cdot d_1$. This is also known from literature; see e.g. the experimental results of Babarutsi, Ganoulis & Chu (1989). Second, from the current PIV experiments, it appears that the dimensionless length L_2/d_1 of the secondary recirculation cell increases for decreasing depth. This is understandable because, as the primary recirculation flow decreases in size, discharge and energy, it will separate more easily from the wall because of the local adverse pressure gradient. Third, an intermittent gyre can exist opposite to the

primary recirculation, approximately opposite to the primary reattachment point. This gyre is caused by large-scale mixing layer vortices that sometimes entrain so much fluid from the main flow that the main flow incidentally separates from the straight wall.

Fourth, a mixing layer is observed downstream of the separation point. The stability and small width of the near-field mixing layer is striking, in spite of the presence of a strong lateral shear between the secondary gyre and the main flow. The small coherent structures emerging from the separation point seem to be almost insensitive to the intense local shear. From the point where the mixing layer touches the primary gyre, at a downstream distance of the order of the expansion width d_1, the structures appear to be amplified in scale significantly. Downstream from this point a considerably stronger fluid entrainment takes place. A pronounced scale jump is visible in cases where the secondary recirculation cell is large in size (L_2/d_1 values larger than e.g. 2). For smaller secondary gyres, the mixing layer development is smoother. In between the far-field large eddies, long streamwise streaks of upwelling and downwelling fluid occur, which is explained by the stretching of the local velocity field which intensifies the (small-scale) vortices at sub-depth scale.

The flow features mentioned above, observed within the PIV data set, are recognized in the results of the corresponding LES computations. Not in all cases, however, the quantitative properties are equal. In the sections below, both datasets are compared.

3.2 LES data analysis: statistics

Time series were obtained from the LES by sampling the velocities every 0.1 s during a period of 1000 s, which is equivalent to approximately 50-80 consecutive large eddies passing through a cross-section in the far field.

Figures 7a to 7f show the time-averaged streamwise surface velocity fields for each of the 3 geometries. The experimental and computational cases are compared. Only a part of the LES domain is shown (expansion area including the secondary recirculation) in order to make a 1-to-1 comparison with the PIV data domain. The main flow is from left to right. It can be seen that the relative length of the secondary gyre L_2/d_1 is largest for the 1:4 geometry. This is the shallowest case where the dimensionless depth h/d_1 is smallest. In each case the predictions of secondary gyre length and secondary gyre discharge are in good agreement despite a slight underprediction. The computed locations of the secondary separation point are rather accurate. This may be called an achievement resulting from the way the wall shear stresses are handled. From the many numerical tests carried out in this study, it is concluded that: a) the boundary layer formulation must be able to handle both no-slip and partial-slip conditions, and b) a momentum-conservative IBM formulation is needed, in order to obtain a correct secondary recirculation regarding strength and size.

In figures 8a to 8f, the horizontal Reynolds stresses $\overline{u'v'}$ at the surface are compared. Quantities like these are harder to compare than mean flow quantities. Because quantities like Reynolds stresses and turbulent kinetic energy are constructed from flow fluctuations, they are sensitive to resolution differences between measurements and simulations. Although the resolutions of the PIV and LES data sets are the same, the PIV analysis essentially contains an interpolation procedure because of the use of interrogation windows. These windows are approximately 100 x 100 mm², while the distance between data points is 24 mm. Hence, some spatial filtering is unavoidable when using PIV, whereas the LES data are resolved on the grid and are not filtered. The PIV spatial filtering has consequences for time series and time statistics: the values of $\overline{u'^2}$, $\overline{v'^2}$ and $\overline{u'v'}$ found in the LES data are exceeding the PIV data values, even up to a factor 2. Although the contours and patterns of the computed quantities are comparable, there is a difference in the velocity scale. In this case, the LES data are likely to be more accurate than the PIV data set because of the better resolution. It can be shown that especially the small turbulence scales account for the big differences. For a fair comparison, a practical adaptation should be made to the LES data set: when

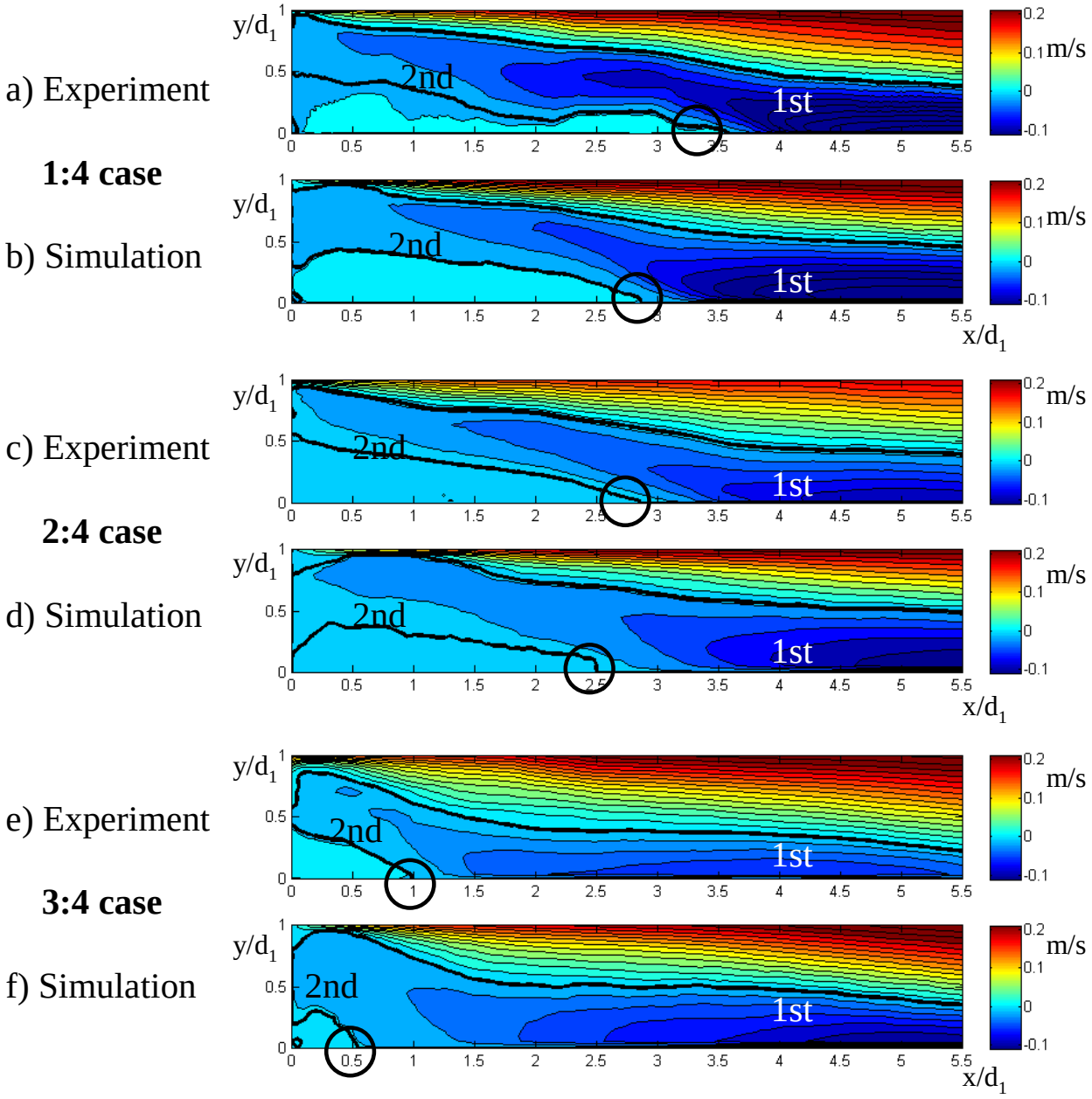

Figure 7a-f Comparison of experimental and computational streamwise velocities at the surface. Black solid lines are zero velocity contours; the black circles are locating the secondary separation points; 1st = location primary gyre; 2nd = location secondary gyre.

the LES velocity fluctuations are filtered using a 100 mm wide top-hat filter, the obtained LES values of $\overline{u'^2}$, $\overline{v'^2}$ and $\overline{u'v'}$ are in better agreement with the PIV data. The illustrations in Figures 8a to 8f show the LES quantities based on this top-hat filtering procedure.

The problem described above can be expected in all cases where small-scale flow fluctuations are retrieved from measurement techniques with a limited resolution or involving some interpolation (like PIV). Large-scale flow fluctuations are represented much better by PIV measurements, which is fortunate because this study focuses on large-scale turbulent structures. Regardless of the resolution problem described above, the patterns are clear. Maximum values are found around a line downstream of each separation point. For the horizontal Reynolds stresses, this is a negative peak because the large eddies have a clockwise vorticity. In the near field only small-scale fluctuations

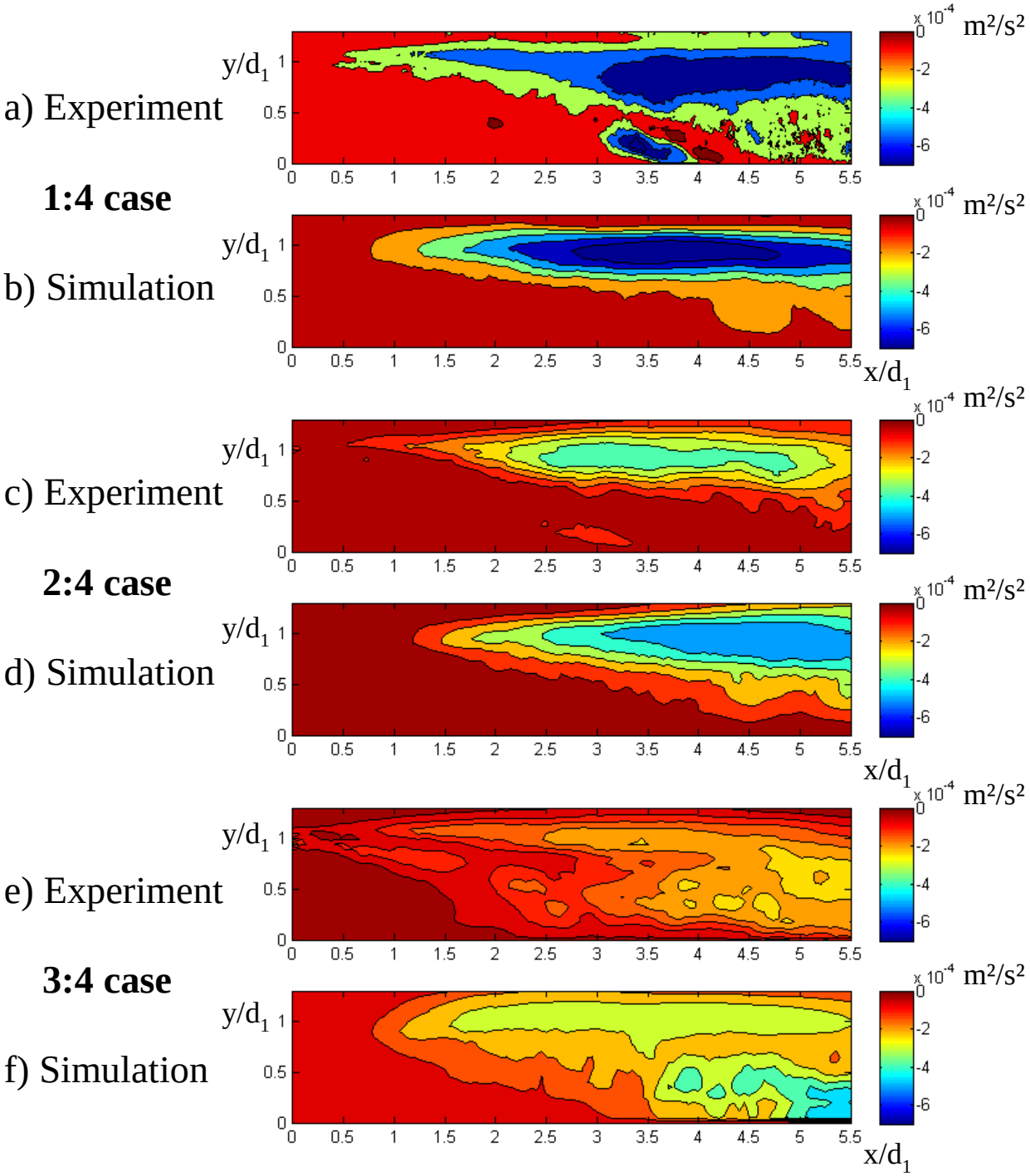

Figure 8a-f Experimental and (filtered) computational horizontal Reynolds stresses (same domain as Figure 7)

are present, whereas the data contours show that the development of large-scale turbulence and increased momentum transfer starts from a point between primary and secondary recirculation: $x/d_1 \approx 1$.

3.3 LES data analysis: length scales and conditional averages

From the computed Reynolds stresses a Prandtl mixing length can be derived. To do this, the time-averaged deformation tensor at the mixing layer centre is computed. In each flow cross-section, the

location of the minimum of the Reynolds stress values has been chosen to determine the mixing length. These locations form an almost straight line downstream of the separation point. A straightforward relation between the horizontal Reynolds stress $\overline{u'v'}$ and Prandtl mixing length λ has been used, which reads:

$$\left|\overline{u'v'}\right| = \lambda^2 \left(\frac{\partial v}{\partial x} + \frac{\partial u}{\partial y} \right)^2 \tag{4}$$

The figures 9a and 9b compare the computed Prandtl mixing lengths at the surface, obtained from the PIV experiments and respective LES simulations. From the latter, the top-hat filtered Reynolds stresses have been used. The solid black lines in both figures are trend lines.

The PIV data show a clear similarity in the mixing length profiles of all three geometries, whereas the 2:4 case shows the most pronounced discontinuity in scale growth. The location of this jump lies around $x/d_1 = 0.8$. The LES data mixing length profiles are much smoother than the PIV profiles, which is true for the filtered LES turbulence properties in general. The profiles of the 1:4 and 3:4 case are more or less in accordance with the PIV data; the 2:4 case profile appears to be considerably underpredicted. All cases show the same pattern: the large turbulence scales emerge from the scale jump location.

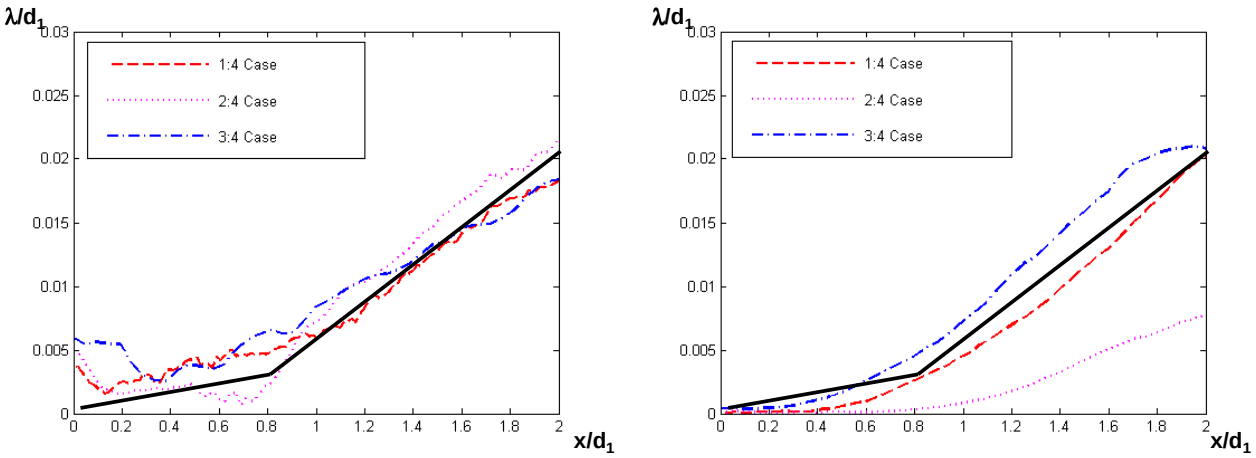

Figure 9a-b Comparison of Prandtl mixing length scales based on horizontal Reynolds stresses, scaled by d_1. Left: PIV experiments, right: (filtered) LES computations. Red dashed line: 1:4 case, magenta dotted line: 2:4 case, blue dash-dot line: 3:4 case, solid black line: suggested trend line

It is not surprising that the above method yields length scales that are much smaller than the actual large-eddy sizes, because time-averaged statistics are used to describe an intermittent phenomenon. The vortex length scale development can better be examined by conditional averaging of the shed vortices. The procedure is described below.

The mixing layer centre is located in the neighbourhood of the straight line downstream of the separation point. For each point along this line, the cross section of the flow is checked for the presence of a large eddy. This is done by searching local minima in the vector potential time series (see Section 2.3), after subtraction of the mean flow pattern. The latter has to be done in order to remove the dominant contributions by the steady recirculations. The velocity maps containing large eddies are stored for further statistical operations. Figure 10a gives an illustration of the results.

Conditional averaging of the spanwise velocity signal is used as the quantity for determining local large-eddy length scales. The spanwise velocity changes sign at the location of conditionally

averaged eddy cores. An eddy length scale can be defined as the distance between the successive centroid locations of the vortex velocity profiles.

Please note that in this study, vector potential functions are used only for detection of large eddies in order to perform the conditional averaging procedure, but they are not suitable as an object of any further data statistics. For determining eddy scales, it is better to turn back to the velocity signal itself. Furthermore, the unfiltered LES data have been used to perform the conditional averaging; there is no need to filter here, because no variance or covariance of the data is involved.

In principle, conditional averaging can be done for every point within the measured flow domain. Obviously, the averaging procedure makes most sense when it is performed along the mixing layer centre line. Far-field mixing layer vortices can be well examined in this way and also their length scales can be determined directly from their conditionally averaged velocity profiles. The near-field, however, is more problematic; the number of data points per wave length of mixing layer vortices is much lower here, resulting in poor statistical results and eddy length scales that are noisy. For the near field, a more robust approach is needed. This can be achieved by determining the passage time scales of conditionally averaged vortices and multiplying these by the propagation speed of the large-eddy core, using Taylor's hypothesis of "frozen turbulence". In this way an "eddy wave length" is obtained; the real eddy size is about 50% of this wave length. Because the examined

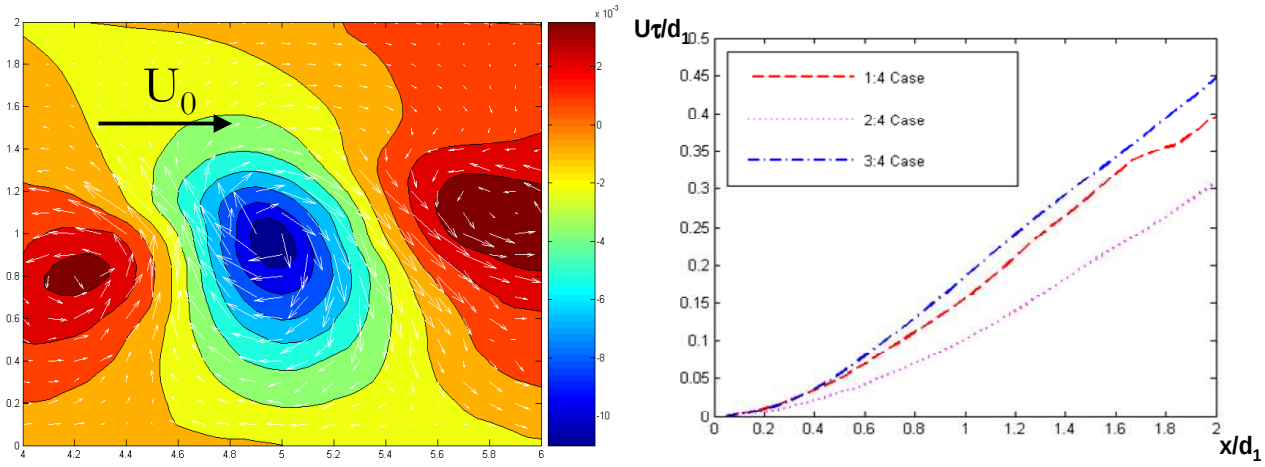

Figure 10a-b Conditional averaging of large-scale coherent structures shed from the separation point. Left: conditionally averaged (unfiltered) velocity field and vector potential function, constructed by approximately 50 consecutive large eddies. Right: spatial development of large-eddy length scales determined using Taylor's hypothesis. Red dashed line: 1:4 case, magenta dotted line: 2:4 case, blue dash-dot line: 3:4 case

turbulent flow is stationary rather than homogeneous, the obtained data are more suitable for temporal than spatial statistics. This approach appears less sensitive to near-field noise and yields a more smooth length scale development, which can be compared with the Prandtl length scales found before.

Figures 10b shows the computed length scales of the dominant eddies caused by vortex shedding, as a function of x/d_1, for each of the 3 LES cases. Both axes are scaled by the lateral expansion width d_1. Please note the order of magnitude being much larger (approximately 15-20 times) than the Prandtl length scales of Figure 9. The eddy sizes are now of the same order of magnitude as the width of the mixing layer. Again, it can be seen that the large-eddy development is starting slowly and is boosted at some distance downstream, although the shift in Figure 10b is more gradual than the jump in the Figures 9a-b.

4. CONCLUSIONS AND APPLICATION

Three-dimensional LES computations of Shallow Lateral Expansion geometries have been performed in order to make a comparison with corresponding experimental PIV results. Special attention was paid to boundary conditions at immersed boundaries in combination with a wall shear stress model. The IBM implementation used here ensures a proper treatment of momentum fluxes near solid walls. The result is a simple but generic formulation. This formulation contributes to de proper simulation of shallow separating flows, especially with respect to the steady recirculation sizes and the location of the secondary separation point.

The large-scale turbulence structures in the flow were visualized by means of a vector potential function. Due to resolution differences between measurements and simulations, as well as the practical difficulty to obtain sufficient PIV resolution, the direct comparison of turbulent kinetic energy and horizontal Reynolds stress is problematic. When a spatial top-hat filter is being applied to the LES turbulence quantities, however, the agreement of measured and simulated quantities is fair. Determining the large-eddy length scales in different ways shows the presence of a scale jump between the near-field and far-field mixing layer. It appears that a simple 3D Smagorinsky subgrid model contributes well to the simulation of quasi-2D turbulence features, such as the spatial development of large-scale coherent structures.

The knowledge obtained on the scale jump phenomenon in shallow separating flows, resulting from both experiments and computations, can be of use for river engineering purposes. Because vortex shedding behaviour is influenced by the presence and strength of a secondary recirculation, the possibility exists to mitigate the large-scale turbulence by manipulating this recirculation. By changing the shallow flow geometry, the secondary recirculation can be altered with respect to size or energy. Especially the shape of the body along which the main flow separates is an important factor, as well as the presence or absence of downstream obstacles. Apart from physical experiments, LES computations are an effective and cheap way of investigating the influence of geometrical changes on large-scale turbulence behaviour. To this end, a number of new shallow separation flow geometries, slightly different from the geometries described in this paper, are currently being studied.

ACKNOWLEDGEMENT

This research is supported by the Dutch Technology Foundation STW, applied science division of NWO and the Technology Programme of the Ministry of Economic Affairs.

REFERENCES

Adrian, R.J., Christensen, K.T. & Liu, Z.-C. (2000). “Analysis and interpretation of instantaneous turbulent velocity fields”, Experiments in Fluids, Vol. 29:275-290.

Babarutsi, S., Ganoulis, J. & Chu, V.H. (1989). “Experimental investigation of shallow recirculating flows”, Journal of Hydraulic Engineering, Vol. 115, No. 7: 906-924.

Babarutsi, S., Nassiri, M. & Chu, V.H. (1996). “Computation of shallow recirculating flow dominated by friction”, Journal of Hydraulic Engineering, Vol. 122, No. 7: 367-372.

Bonnet, J.P., Delville, J. et al. (1998). “Collaborative testing of eddy structure identification methods in free turbulent shear flows”, Experiments in Fluids, Vol. 25: 197-225.

Breugem, W.P. (2004). The Influence of Wall Permeability on Laminar and Turbulent Flows, Ph.D. Thesis, Delft University of Technology, pp. 67-69, 142-145.

Fadlun, E.A., Verzicco, R., Orlandi, P. and Mohd-Yusof, J. (2000). "Combined Immersed-Boundary Finite-Difference Methods for Three-Dimensional Complex Flow Simulations", Journal of Computational Physics 161, pp. 35–60

Mittal, R. and Iaccarino, G. (2005). "Immersed Boundary Methods", Annual Review of Fluid Mechanics, 37, pp. 239-261

Neto, A.S., Grand, D., Métais, O. and Lesieur, M. (1993). "A numerical investigation of the coherent vortices in turbulence behind a backward-facing step" Journal of Fluid Mechanics, Vol. 256, pp. 1-25

Prooijen, B.C. van (2004). "Shallow Mixing Layers", Ph.D. Thesis Delft University of Technology, Delft, pp. 17-20

Scarano, F., Benocci, C. & Riethmuller, M.L. (1999). "Pattern recognition analysis of the turbulent flow past a backward facing step", Physics of Fluids, Vol. 11, No. 12: 3808-3818.

Talstra, H., Uijttewaal, W.S.J. and Stelling, G.S. (2006). "Emergence of large-scale coherent structures in a shallow separating flow", Conference proceedings of River Flow 2006, International Conference on Fluvial Hydraulics, Lisboa, 6-8 September 2006, pp. 261-269.

Tessicini, F. Iaccarino, G., Fatica, M., Wang, M. and Verzicco, R. (2002). "Wall modeling for large-eddy simulation using an immersed boundary method", Center for Turbulence Research, Annual Research Briefs 2002, pp. 181-187

Uijttewaal, W.S.J., Lehmann, D. & Van Mazijk, A. (2001). "Exchange processes between a river and its groyne fields: model experiments", Journal of Hydraulic Engineering, Vol. 127, No. 11: 928-938.

APPENDIX: VECTOR POTENTIALS

Given a 3d solenoidal velocity vector field:

$$\vec{u} = (u, v, w) \text{, with } \nabla \cdot \vec{u} = 0 \text{ and } \nabla \times \vec{u} = \vec{\omega} \tag{i}$$

For such a vector field, a vector potential $\vec{\psi}$ exists such that

$$\vec{u} = \nabla \times \vec{\psi}\,, \tag{ii}$$

Since by definition $\nabla \cdot \nabla \times \vec{\psi} = 0$. Please note that $\vec{\psi}$ is determined apart from an arbitrary gradient field $\nabla\phi$, because $\vec{\psi}' = \vec{\psi} + \nabla\phi$ is also satisfying equation (ii).
The vorticity $\vec{\omega}$ now can be written as

$$\vec{\omega} = \nabla \times \left(\nabla \times \vec{\psi} \right) = \nabla \left(\nabla \cdot \vec{\psi} \right) - \nabla^2 \vec{\psi} \tag{iii}$$

Because $\vec{\psi}$ has a degree of freedom, it can be chosen such that $\vec{\psi}$ is also solenoidal. In that case, expression (iii) for the vorticity reduces to a Poisson equation:

$$\vec{\omega} = -\nabla^2 \vec{\psi} \tag{iv}$$

The wonderful thing about the Laplacian operator in this expression is that it operates on each vector component separately. Therefore, if only one component of the vorticity is known, yet the full z-component of the vector potential can be constructed. In this study, the emphasis is on the vertical

vorticity component ω_z, that is made up by horizontal surface velocities u and v. At the velocity field edges, it is sufficient to use homogeneous Neumann boundary conditions for solving the Poisson equation.

Taking the curl of the constructed vector potential component ψ_z yields in turn a vector field that practically resembles the original velocity field (u,v). It only differs slightly from the original velocity field because a 2D plane within a 3D flow has a nonzero divergence. Therefore, the vector potential function ψ_z only makes sense if the flow is quasi-2D. This condition is obviously satisfied in case of a shallow flow with large coherent structures in the horizontal plane. In that case, taking the curl of the vector potential is practically equivalent to:

$$u = \partial \psi_z / \partial y \text{ and } v = -\partial \psi_z / \partial x, \tag{v}$$

which shows that ψ_z very much resembles a 2D stream function of (u,v), except for the fact that an important correction has been made to circumvent the nonsolenoidality of the (u,v)-plane.

In fact, computing a vector potential is a way to *integrate* the associated velocity field, revealing large-scale rotation patterns. On the contrary, computing a vorticity means taking a *derivative* of that velocity field, effectively favouring small-scale rotation patterns. This explains why vorticity data are often very noisy while, on the other hand, vector potential data are quite smooth and hence much easier to interpret.

Each local maximum or minimum of a vector potential function identifies a vortex core of positive respectively negative vorticity sign. The function isolines are very well parallel to the original vector field. It may be concluded that vector potentials are a most suitable tool for identifying large eddies.